15. M. Türler, T. J.-L. Courvoisier, S. Paltani, *Astron. Astrophys.* **349**, 45 (1999).
16. A. P. Marscher, *Astrophys. J.* **235**, 386 (1980).
17. J. L. Gómez, A. Alberdi, J. M. Marcaide, *Astron. Astrophys.* **274**, 55 (1993).
18. ———, *Astron. Astrophys.* **284**, 51 (1994).
19. J. L. Gómez, A. Alberdi, J. M. Marcaide, A. P. Marscher, J. P. Travis, *Astron. Astrophys.* **292**, 33 (1994).
20. A. J. Mioduszewski, P. A. Hughes, D. G. Comer, *Astrophys. J.* **476**, 649 (1997).
21. P. E. Hardee, *Astrophys. J.* **287**, 523 (1984).
22. ———, *Astrophys. J.* **303**, 111 (1986).
23. ———, *Astrophys. J.* **313**, 607 (1987).
24. ———, D. A. Clarke, A. Rosen, *Astrophys. J.* **485**, 533 (1997).
25. P. E. Hardee, *Astrophys. J.* **533**, 176 (2000).
26. J. A. Zensus, P. D. Diamond, P. J. Napier, Eds., *Very Long Baseline Interferometry and the VLBA, ASP Conference Series*, vol. 82 (Astronomical Society of the Pacific, San Francisco, 1995).
27. H. Hirabayashi *et al.*, *Science* **281**, 1825 (1998).
28. H. Hirabayashi *et al.*, *Publ. Astron. Soc. Jpn.* **52**, 955 (2000).
29. HALCA is the Highly Advanced Laboratory for Communications and Astronomy.
30. The Very Long Baseline Array is operated by the National Radio Astronomy Observatory, USA.
31. The Effelsberg 100-m telescope is operated by Max-Planck-Institut für Radioastronomie, Bonn, Germany.
32. A. P. Lobanov *et al.*, *Adv. Space Res.* **26**, 669 (2000).
33. A. P. Lobanov, T. P. Krichbaum, A. Witzel, J. A. Zensus, *New Astron. Rev.* **43**, 741 (1999).
34. M. A. Strauss *et al.*, *Astrophys. J. Suppl.* **83**, 29 (1992).
35. At distances from the jet origin larger than 12 mas, the profiles show evidence for even more complex structure, with perhaps a third, weaker and more extended emitting component inside the jet (as seen, for instance, in the profile "D" plotted in the inset of Fig. 1). The spatial sampling of the VSOP data does not permit us to determine unambiguously the peak and the size of such extended features, and this limits our present study to measuring the properties of the two stronger features inside the jet.
36. The position offsets of the threads P1 and P2 are first calculated with respect to a fixed jet axis, and then a precession term is introduced. The position angle of the jet axis, $\Phi_j = -138°$, is estimated from the available images of kiloparsec-scale structures in 3C273 (*8*). The precession wavelength, $\lambda_{prec} = 100 \pm 20$ mas, is estimated from high dynamic range VLBI images of 3C273 (*10*). With the precession term applied, we proceed to determine the minimum number of sinusoidal modes necessary to represent the observed locations of the threads P1 and P2.
37. The evolution of a sinusoidal mode is described by an amplitude term $G_j(z) = a_j(2ze^{1-z/z_j})/(z + z_j)$, where z is the coordinate along the jet axis. The corresponding position offset introduced by the mode in the picture plane is $r_j(z) = G_j(z)\cos\{\psi_j + 2\pi z[\lambda_j(1 + z\sin\phi_j)]^{-1}\}$, where ϕ_j describes the half-opening angle of the jet.
38. If λ^* is substantially different in one of the modes, it would indicate that either (i) the fitted wavelength of the mode has a large error, (ii) the mode has been identified incorrectly, or (iii) the mode does not grow at its resonant wavelength (for instance, if is driven externally or develops at a longer wavelength not exceeding the longest unstable wavelength).
39. The resulting basic relations are $\lambda^* = [8R_jM_j\Gamma_j \sin\theta]/[1 + \eta^{0.5}/\delta_j]$ and $P_o = [(1 + z)\lambda_1(1 + \eta^{0.5}/\delta_j)]/[\beta_j\delta_j \sin\theta\,(1 + \eta^{0.5}\Gamma_j)]$, where $\delta_j = 1/[\Gamma_j(1 - \beta_j \sin\theta)]$ is the Doppler factor of the jet.
40. We thank P. E. Hardee and I. K. K. Pauliny-Toth for helpful discussions and comments on the manuscript. We gratefully acknowledge the VSOP Project, which is led by the Japanese Institute of Space and Astronautical Science in cooperation with many agencies, institutes, and observatories around the world. The National Radio Astronomy Observatory is a facility of the NSF operated under cooperative agreement by Associated Universities.

7 June 2001; accepted 24 August 2001

Ferromagnetic Imprinting of Nuclear Spins in Semiconductors

R. K. Kawakami,[1] Y. Kato,[1] M. Hanson,[2] I. Malajovich,[1] J. M. Stephens,[2] E. Johnston-Halperin,[1] G. Salis,[1] A. C. Gossard,[2] D. D. Awschalom[1]*

We examine how a ferromagnetic layer affects the coherent electron spin dynamics in a neighboring gallium arsenide semiconductor. Ultrafast optical pump-probe measurements reveal that the spin dynamics are unexpectedly dominated by hyperpolarized nuclear spins that align along the ferromagnet's magnetization. We find evidence that photoexcited carriers acquire spin-polarization from the ferromagnet, and dynamically polarize these nuclear spins. The resulting hyperfine fields are as high as 9000 gauss in small external fields (less than 1000 gauss), enabling ferromagnetic control of local electron spin coherence.

Investigations of electron spins in solids have led to several important discoveries such as giant magnetoresistance in metallic magnetic multilayers (*1*) and long spin-coherence times in semiconductors (~100 ns) (*2*). The recent development of layered ferromagnet/semiconductor heterostructures (*3–7*) enables integration of these approaches to spintronics, and presents new possibilities for controlling coherent electron spin dynamics in semiconductors through manipulation of the local magnetic environment. For instance, it is thought that effective magnetic fields generated by a ferromagnet could be exploited to change the quantum state of selected electron spins, while leaving others undisturbed (*8*). To develop this type of "quantum magnetoelectronics" it is necessary to explore how such ferromagnetic layers affect the electron spin dynamics in nearby semiconductors.

We report that the electron spin dynamics in an *n*-type GaAs layer are strongly modified by an adjacent ferromagnetic layer. Unexpectedly, the dominant interaction is identified as hyperfine coupling with nuclear spins in GaAs (*9–11*), and not fringe fields or direct exchange interactions with the ferromagnet. To investigate the electron spin dynamics, we used the pump-probe technique of time-resolved Faraday rotation (TRFR) (*12*) to measure the precession of optically generated electron spins in a transverse magnetic field. Using the precession frequency as a sensitive magnetometer of the total field in the GaAs layer, we found that the ferromagnetic layer produces local fields as high as 9000 G in an applied field of 1000 G. These local fields follow the magnetic hysteresis loop of the ferromagnetic layer except near zero applied field, where they vanish despite the presence of significant remanent magnetization. A series of measurements demonstrate that this local field arises from an unanticipated process: ferromagnetic imprinting of nuclear spins. In this carrier-mediated process, the ferromagnetic layer induces nuclear spin polarization in the adjacent GaAs layer along the local magnetization, leading to effective magnetic fields which act on the electron spins in GaAs through the hyperfine interaction (*9*). Thus, the dynamics of the optically generated electron spins can be controlled by a ferromagnet through the creation of a ferromagnetic imprint in the GaAs nuclear spin system.

Samples were grown by molecular beam epitaxy and had the following structure: ferromagnet/*n*-GaAs/$Al_{0.75}Ga_{0.25}As$/n^+-GaAs(100) substrate. All layers up to the ferromagnet were grown in a separate chamber to maximize the optical quality of the 100-nm *n*-GaAs layer (Si: 7×10^{16} cm^{-3}). Four samples were prepared (*13*), each with a different ferromagnetic layer and Curie temperature T_C: 25-nm type-A MnAs ($T_C \sim 320$ K) (*3*), 15-nm (Ga,Mn)As with ~5% Mn concentration ($T_C \sim 75$ K) (*4*), five-period digital ferromagnetic heterostructure (DFH) of ½ monolayer (ML) MnAs spaced by 10 ML GaAs ($T_C \sim 60$ K) (*6*), and ½ ML MnAs (henceforth termed "single layer") ($T_C \sim 55$ K) (*6*). The last three samples were capped with 20 ML of GaAs. We also prepared a control sample without a ferromagnetic layer. Each sample was mounted on fused silica with transparent epoxy and the substrates were removed up to the 400-nm AlGaAs layer by a selective etch (*14*).

The samples were placed inside a magneto-optical cryostat and electron spin dynamics in the GaAs layer were investigated by TRFR (*12*). Our pump-probe experiments used short

[1]Department of Physics and [2]Materials Department, University of California, Santa Barbara, CA 93106, USA.

*To whom correspondence should be addressed. E-mail: awsch@physics.ucsb.edu

laser pulses tuned to the band gap of GaAs and focused to a ~50 μm diameter spot. A circularly polarized pump pulse incident normal to the sample created spin-polarized electrons in the GaAs layer. After a time delay Δt, the normal component of net spin throughout the GaAs layer was measured by Faraday rotation θ_F of a linearly polarized probe pulse, which is about 10 times weaker than the pump pulse. The temporal evolution of the electron spin was obtained by measuring θ_F while scanning Δt. Unless otherwise noted, the pump beam has an average intensity of ~35 W/cm^2 (for ~100-fs pulses with 76 MHz repetition rate) and its helicity is modulated at 50 kHz by a photoelastic modulator (PEM) for lock-in detection. Applying an in-plane magnetic field B_{app} causes the optically generated electron spins to precess about the field at the Larmor frequency $\nu_L = g\mu_B B_{tot}/h$, where g is the electron g-factor, μ_B is the Bohr magneton, and the total field B_{tot} is the sum of B_{app} and local effective fields B_{loc} that may arise from one or more of the following sources: fringe fields from the ferromagnetic layer, direct exchange interaction with magnetic moments (*12*), and hyperfine interaction with nuclear spins (*10*).

For all samples, we measured TRFR time scans at 5 K with an applied field of 1000 G along an in-plane magnetic easy axis (Fig. 1). Using the control sample as a reference (*15*), we observed that the ferromagnetic layer causes electron spins to precess with a significantly increased Larmor frequency, corresponding to local fields of 1300 G (single layer), 2100 G (DFH), 2500 G [(Ga,Mn)As], and 7000 G (MnAs). The dependence of Larmor frequency on applied field is determined by measuring the TRFR time scans for a series of B_{app}. As shown for the single-layer sample, B_{app} was swept from –1000 G to 1000 G in steps of 10 G (Fig. 2A). The time interval between field steps is ~40 s, the time needed to obtain each TRFR scan. Near 250 G, we observed a sharp change in the Larmor frequency, corresponding to a magnetization reversal as revealed in the magnetic hysteresis loop obtained by magneto-optic Kerr effect (MOKE) measurements (Fig. 2C, upper panel). Figure 2B shows the TRFR as the field sweep is reversed, and the sharp change appears near –250 G.

This measurement procedure was repeated for each of the samples, and the results are summarized in Fig. 2, C through F. The Larmor frequency ν_L is determined by fitting data at each applied field with $\theta_F = A\exp(-\Delta t/T_2^*)\cos(2\pi\nu_L\Delta t)$, where T_2^* is the effective transverse spin lifetime. For all samples, the sharp change in ν_L occurs when B_{app} matches the coercive field observed in the magnetic hysteresis loop. This is a clear indication that the ferromagnetic layer strongly influences the electron spin dynamics. The gradual switching of ν_L after magnetization reversal ($B_{app} > 1000$ G) in Fig. 2F deserves special attention. As confirmed by control measurements (*16*), magnetization reversal induces a continuous evolution in ν_L that requires ~20 min to reach the steady state (*17*). Although this effect is strongest for the MnAs sample, laboratory time dependence was observed in all samples (*18*).

As B_{app} approaches zero, ν_L vanishes (*19*) in all samples despite the significant remanent magnetization of the ferromagnet. The presence of this "dip" cannot be explained in terms of either fringe field effects or direct exchange interactions with the magnetic moments. These mechanisms predict a replication of the magnetization curves superimposed upon a linear background from the usual Zeeman contribution, in contradiction to the observed behavior of ν_L.

To simultaneously account for the hysteresis in $\nu_L(B_{app})$, the observed lab time dependence (on the order of minutes), and the zero-field dip, we propose the following model: nuclear spins in the GaAs layer are dynamically polarized along the magnetization of the neigh-

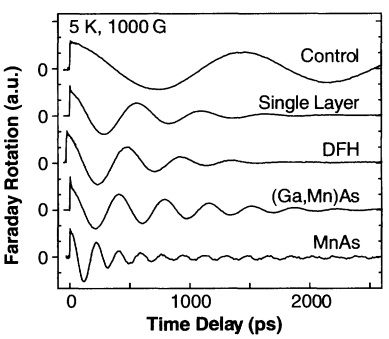

Fig. 1. Time-resolved Faraday rotation (TRFR) time scans taken at 5 K with a 1000 G magnetic field. The four ferromagnetic samples exhibit a higher Larmor precession frequency compared to the control sample, indicating that the ferromagnet generates an effective magnetic field which acts on coherent electron spins in the GaAs layer. The curves are vertically offset for clarity.

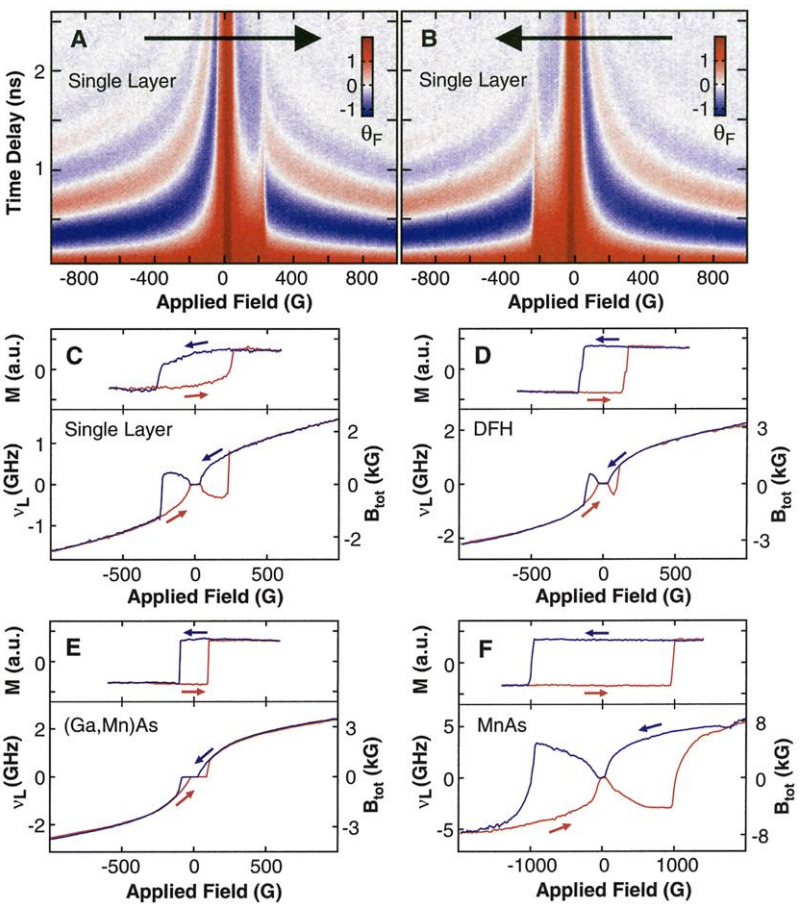

Fig. 2. (A and B) On the single-layer sample, sequential TRFR time scans are taken at 5 K as the applied magnetic field is (**A**) ramped up from –1000 G to 1000 G in 10 G steps, and (**B**) ramped down from 1000 G to –1000 G. The amplitude of rotation θ_F is represented by the color. (**C**) Top: Magnetic hysteresis loop of the single layer sample at 5 K, measured by the magneto-optic Kerr effect (MOKE). Bottom: Larmor frequency as a function of field, obtained by fitting the TRFR time scans in (A) and (B) at each applied field. The red curve is from the up sweep (A) and the blue curve is from the down sweep (B). (D through F) MOKE hysteresis loop and Larmor frequency as a function of field at 5 K for the (**D**) DFH sample, (**E**) (Ga,Mn)As sample, and (**F**) MnAs sample. The field step in (D) through (F) is 20 G.

boring ferromagnetic layer, and the resulting nuclear polarization generates effective fields, B_{loc}, which act on electron spins through the hyperfine interaction (*9*). In this model, the hysteresis in ν_L occurs because the nuclear polarization depends on the magnetization, the observed lab time dependence is characteristic of nuclear polarization (*9, 10*), and the vanishing of ν_L near zero-field is attributed to a suppression of nuclear polarization. Similar zero-field behavior has been observed in bulk *p*-GaAs where nuclear dipole-dipole interactions suppress polarization below ~2 G (*9, 20*). In our case, however, the half-width of the dip ranged from 100 to 200 G, suggesting that additional mechanisms contribute to the suppression (*21*); this is currently under investigation. The dip also shows that the effect of fringe fields and direct exchange are negligible because it is centered at $B_{app} = 0$ G and ν_L goes to zero (*19*).

The temperature dependence of ν_L is also consistent with the presence of nuclear polarization (Fig. 3A). At 1000 G, ν_L drops with increasing temperature and approaches the value of the control sample at ~60 K for all samples. Because the remanent magnetization M_R of MnAs shows little decrease with temperature T (Fig. 3A, inset), the drop in ν_L cannot be explained by $M_R(T)$. On the other hand, the observed $\nu_L(T)$ is consistent with dynamic nuclear polarization in bulk GaAs (*10*) and GaAs quantum wells (*11*), where the nuclear polarization vanishes at ~30 and ~80 K, respectively.

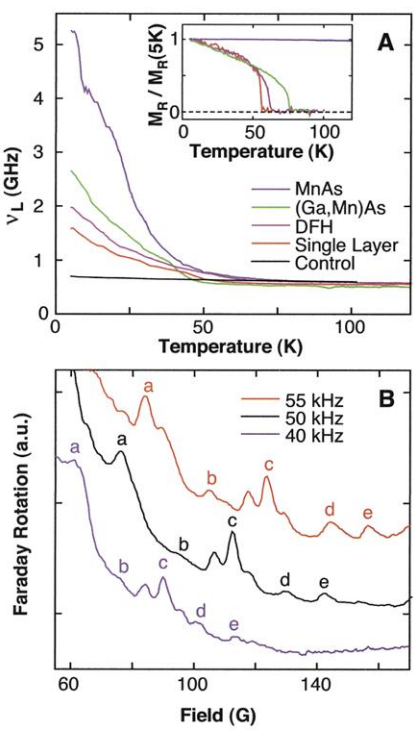

Fig. 3. (**A**) Temperature dependence of Larmor frequency at 1000 G. (Inset) Remanent magnetization as a function of temperature measured by superconducting quantum-interference device magnetometry. (**B**) All-optical NMR performed on the single-layer sample at 5 K. The Faraday rotation is measured as a function of field at Δt = 1500 ps for three different fundamental frequencies of the PEM. The curves are vertically offset and scaled for clarity. Resonance peaks **b** and **e** are identified as the second and third harmonics of ^{69}Ga, **a** and **c** are identified as the second and third harmonics of ^{71}Ga, and **d** is identified as the second harmonic of ^{75}As.

Direct evidence of nuclear polarization is found by showing that ν_L can be decreased by resonantly depolarizing the nuclear isotopes of the GaAs semiconductor. This is accomplished through all-optical nuclear magnetic resonance (NMR) (*10, 11, 22*) performed in the field range of interest (<500 G). The PEM modulates the helicity of the pump beam at a given fundamental frequency (f = 40, 50, or 55 kHz), resulting in a modulation of the optically generated electron-spin polarization. This leads to an effective ac-magnetic field through the hyperfine interaction. The nuclear spins depolarize when the resonance condition $\gamma B_{app} = nf$ is met, where γ is the isotope-specific gyromagnetic ratio and n is an integer labeling the harmonics of the PEM modulation. On the single-layer sample, we measured the Faraday rotation θ_F as a function of the field for each PEM frequency at Δt = 1500 ps (Fig. 3B). We observed peaks that shift with PEM frequency, as expected from the resonance condition, and which can be associated with the isotopes ^{69}Ga (γ = 13.0204 MHz/T), ^{71}Ga (γ = 10.2475 MHz/T), and ^{75}As (γ = 7.3148 MHz/T) (*23*). These peaks originate from a reduction in ν_L due to the resonant depolarization of nuclear spins (*11*).

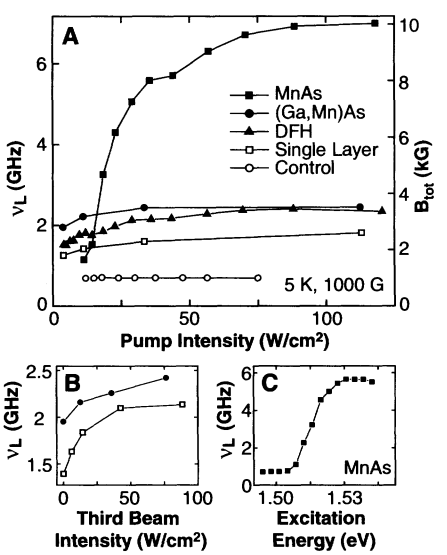

Fig. 4. (**A**) Dependence of Larmor frequency on the intensity of the pump beam. All ferromagnetic samples show increasing frequency with higher intensity, but the control sample does not. (**B**) Dependence of Larmor frequency on the intensity of a linearly polarized third beam for (Ga,Mn)As (filled circles) and single layer sample (open squares). The pump intensity is 3 W/cm^2. (**C**) Dependence of Larmor frequency on the excitation energy of the pump/probe beams for the MnAs sample. The sharp rise in Larmor frequency coincides with the band edge of GaAs.

Having established the presence of nuclear spin polarization in the GaAs layer, we now focus on how the nuclear spins become polarized. The large magnitude of the observed nuclear polarization—approximately 13%, inferred from the 7000 G local field in the MnAs sample (*20*)—suggests that the nuclear spins become polarized by dynamic nuclear polarization (DNP) (*24, 25*). In DNP, nonequilibrium electron spins relax to equilibrium by transferring some of their angular momentum to the nuclear spins via the hyperfine interaction, leading to hyperpolarization of the nuclei. In contrast, a fringe field of >1000 T would be needed to achieve 13% nuclear polarization in thermal equilibrium at 5 K.

A characteristic of DNP is a strong dependence on pump intensity. We found that in all samples, ν_L increases with pump intensity (Fig. 4A), suggesting that the nuclear polarization depends on the concentration of photoexcited carriers. Because the pump pulse is circularly polarized, its intensity controls both the number of carriers and the number of spins. To disentangle these two effects, we lowered the pump beam intensity to 3 W/cm^2 to minimize the creation of spins and focused a linearly polarized third beam with higher intensity onto the same spot on the sample. A similar increase in ν_L with third beam intensity (Fig. 4B) indicates that the helicity of the pump beam is unimportant for generating this nuclear polarization. In addition, by varying the photon energy, we show that the relevant photoexcitation is in the GaAs layer. The sharp increase in ν_L at the band gap of GaAs for the MnAs sample (Fig. 4C) reveals that the relevant carriers are created in GaAs. This distinction is possible, because the optical properties of metallic MnAs differ significantly from GaAs (*26*), in contrast to the GaAs-based ferromagnetic layers used in the other samples.

Distinct from traditional DNP is the dependence of the nuclear spin direction on the ferromagnetic magnetization rather than on the helicity of the pump beam (*11, 25*). Furthermore, optical orientation transverse to the field cannot account for the observed magnitude of nuclear spin polarization (*9, 10*). Efficient DNP at low magnetic fields is only possible if nonequilibrium spins are injected along the field (*25*). This suggests that the nonequilibrium electron spins driving the DNP follow the magnetization of the ferromagnetic layer. This was verified experimentally by exploiting the strong in-plane uniaxial magnetic anisotropy on the MnAs sample, which effectively fixes the magnetization along a single in-plane easy axis (Fig. 5, A and B). Rotating the sample in-plane by an

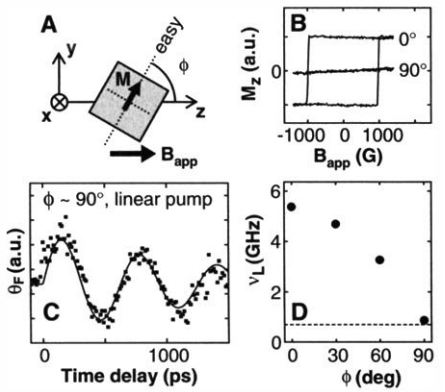

Fig. 5. (**A**) Schematic drawing: the MnAs sample is rotated in-plane to create an angle ϕ between the easy axis and the applied field. (**B**) MOKE hysteresis loops taken with magnetic field applied along the easy axis (ϕ = 0°) and the hard axis (ϕ = 90°) of the MnAs sample. The hard axis loop shows a negligible magnetization component along the applied field, indicating that the magnetization direction remains very close to the easy axis even in the presence of a non-collinear applied field. (**C**) Linearly pumped TRFR time scan at 5 K with $\phi \sim 90°$ and B_{app} = 1000 G. The pump intensity is ~100 W/cm^2. The presence of spin-precession indicates that the ferromagnet polarizes some fraction of the photoexcited electrons along the magnetization. The solid line is a guide to the eye. (**D**) The Larmor frequency at 5 K, 1000 G for different angles ϕ, measured by standard (circularly pumped) TRFR. The dashed line represents the spin precession due to the applied field (Zeeman), and the additional frequency is a measure of the nuclear polarization.

angle $\phi \sim 90°$ causes the magnetization to orient perpendicular to the applied field, while maintaining the normal incidence of the pump beam. In this sample geometry, a linearly polarized pump pulse is used in place of the circularly polarized pump pulse in the TRFR measurement so that the optical excitation imparts no angular momentum to the sample. However, a time scan with B_{app} = 1000 G exhibits precession of coherent electron spins (Fig. 5C) (*27*), indicating that these electrons acquire a component of spin-polarization perpendicular to the field (i.e., along the magnetization). Because this angular momentum does not originate from the pump pulse, it demonstrates that the ferromagnet polarizes some fraction of the photoexcited electrons along the magnetization. Currently, it is unclear how the ferromagnet polarizes the photoexcited electrons; some possibilities include polarization during the absorption process, spin-dependent recombination with spin-polarized holes, and spin-dependent scattering at the ferromagnetic interface. Nonetheless, this result implies that photoexcited electrons mediate the transfer of angular momentum from the ferromagnet to the nuclear spins in GaAs.

Finally, we show that the nuclear polarization depends primarily on the component of magnetization parallel to the applied field. The angle ϕ between the magnetization **M** and $\mathbf{B}_{app}$ is varied systematically by rotating the sample in-plane (Fig. 5A). Returning to TRFR measurement with a circularly polarized pump pulse, ν_L is measured for several angles ϕ (Fig. 5D), and the nuclear polarization corresponds to ν_L in excess of the Zeeman contribution (dashed line). As the parallel component of magnetization vanishes at ϕ = 90°, the nuclear polarization also approaches zero. This behavior is explained by considering the components of electron spin involved in DNP. The circularly polarized pump induces electron spin S_x normal to the sample (axes defined in Fig. 5A). The ferromagnet induces in-plane spin-polarization both parallel to the field $S_z \sim M_z \sim \cos\phi$ and perpendicular to the field $S_y \sim M_y \sim \sin\phi$. DNP depends primarily on the projection of the total electron spin on $\mathbf{B}_{app}$ (i.e., S_z) (*9*), explaining why M_z is the most important component for generating nuclear polarization.

References and Notes

1. M. N. Baibich *et al.*, *Phys. Rev. Lett.* **61**, 2472 (1988).
2. J. M. Kikkawa, D. D. Awschalom, *Phys. Rev. Lett.* **80**, 4313 (1998).
3. M. Tanaka *et al.*, *Appl. Phys. Lett.* **65**, 1964 (1994).
4. H. Ohno, *Science* **281**, 951 (1998).
5. Y. Ohno *et al.*, *Nature* **402**, 790 (1999).
6. R. K. Kawakami *et al.*, *Appl. Phys. Lett.* **77**, 2379 (2000).
7. H. Ohno *et al.*, *Nature* **408**, 944 (2000).
8. D. P. DiVincenzo, *J. Appl. Phys.* **85**, 4785 (1999); D. Loss, D. P. DiVincenzo, *Phys. Rev. A* **57**, 120 (1988).
9. F. Meier, B. P. Zakharchenya, Eds., *Optical Orientation* (North-Holland, New York, 1984).
10. J. M. Kikkawa, D. D. Awschalom, *Science* **287**, 473 (2000).
11. G. Salis *et al.*, *Phys. Rev. Lett.* **86**, 2677 (2001).
12. S. A. Crooker, J. J. Baumberg, F. Flack, N. Samarth, D. D. Awschalom, *Phys. Rev. Lett.* **77**, 2814 (1996).
13. Growth conditions for ferromagnetic layers: T_{growth} = 240°C (MnAs) or 260°C [(Ga,Mn)As, DFH, single layer]; As$_4$/Ga flux ratio ~25; GaAs rate ~5 nm/min; MnAs rate ~0.3 nm/min.
14. H. Tanobe, F. Koyama, K. Iga, *Jpn. J. Appl. Phys.* **31**, 1597 (1992).
15. The *n*-GaAs control sample has g = −0.50.
16. Supplemental figure is available at www.sciencemag.org/cgi/content/full/294/5540/131/DC1.
17. This evolution of ν_L includes a zero-crossing at ~2 min after reversal, which indicates that ν_L changes sign (i.e., spin precession changes direction) in response to a magnetization reversal.
18. Therefore, the exact shape of the ν_L curves in Fig. 2 depends on the field step and acquisition rate.
19. As ν_L approaches zero, its value cannot be resolved below 0.1 GHz due to the limited range of Δt (0 to 2600 ps) accessible by the delay line.
20. D. Paget, G. Lampel, B. Sapoval, V. I. Safarov, *Phys. Rev. B* **15**, 5780 (1977).
21. D. Gammon *et al.*, *Phys. Rev. Lett.* **86**, 5176 (2001).
22. V. K. Kalevich, *Sov. Phys. Solid State* **28**, 1947 (1986).
23. D. R. Lide, Ed., *CRC Handbook of Chemistry and Physics* (CRC Press, Boca Raton, FL, 1993).
24. A. W. Overhauser, *Phys. Rev.* **92**, 411 (1953).
25. G. Lampel, *Phys. Rev. Lett.* **20**, 491 (1968).
26. K. Bärner, R. Braunstein, E. Chock, *Phys. Status Solidi B* **80**, 451 (1977).
27. R. J. Epstein, *et al.*, in preparation.

28. We would like to thank J. English for technical assistance and acknowledge support from Defense Advanced Research Projects Agency, the Office of Naval Research, the Air Force Office of Scientific Research, and NSF.

6 June 2001; accepted 20 August 2001

Spatiotemporal Addressing of Surface Activity

Janpeter Wolff,[1] Athanasios G. Papathanasiou,[1] Ioannis G. Kevrekidis,[2]* Harm Hinrich Rotermund,[1,2] Gerhard Ertl[1]

We have modified surface catalytic activity in real time and space by focusing an addressable laser beam to differentially heat a platinum (110) single-crystal surface. Ellipsomicroscopy imaging of local conditions (such as reactant and product local coverages) enabled us to close the loop between sensing and actuation (both spatiotemporally resolved). Pulses and fronts, the basic building blocks of patterns, could be formed, accelerated, modified, guided, and destroyed at will. Real-time image processing and feedback allow the design and implementation of new classes of nonlocal evolution rules.

The interaction of reaction and transport can lead to pattern formation in reacting systems. Influencing the spatiotemporal pathway of chemical reactions is an active area of research in many branches of science and engineering, from cell biology (*1*) to industrial reactor design (*2*). Overall behavior can be altered by changing the system size (*3–5*), by forcing through an external periodic perturbation (*6*), or simply by feedback (*7*, *8*). We have now connected spatially distributed sensing with locally resolved actuation to form a spatiotemporally addressable catalytic medium for CO oxidation.

During the last decade, pattern formation for several catalytic reactions (such as CO + O_2, NO + CO, NO + H_2, and H_2 + O_2) has been studied over wide ranges of operating condi-

[1]Fritz-Haber-Institut der Max-Planck-Gesellschaft, Faradayweg 4-6, 14195 Berlin, Germany. [2]Department of Chemical Engineering, Princeton University, Princeton, NJ 08544, USA.

*To whom correspondence should be addressed. E-mail: yannis@princeton.edu